Chemical Geology 467 (2017) 30–41

Contents lists available at ScienceDirect

Chemical Geology

journal homepage: www.elsevier.com/locate/chemgeo

Improved spatial resolution of elemental maps through inversion of LA-ICP-MS data

Matthew Fox[a,b,c,*], Alka Tripathy-Lang[a,b], David L. Shuster[a,b]

[a] Department of Earth and Planetary Science, University of California, Berkeley, CA, USA
[b] Berkeley Geochronology Center, Berkeley, CA, USA
[c] Department of Earth Sciences, University College London, United Kingdom

ARTICLE INFO

Keywords:
Laser ablation ICP-MS
Geochemical mapping
(U-Th)/He dating
Magma history
Apatite ^{4}He/^{3}He thermochronometry

ABSTRACT

Laser ablation inductively coupled plasma mass spectrometry (LA-ICP-MS) provides the spatial distribution of elements within crystals and therefore can constrain the rates of geological processes. Spatial resolution of LA-ICP-MS is limited by the requirement to ablate sufficient material to surpass the detection limit of the instrument: too little material and the concentration cannot be measured; too much material from the same spatial location and the possibility of depth dependent variations in concentration increases. Because of this requirement and typical analytical setup, this commonly places a lower bound on the diameter of an ablation 'spot' size of approximately 20 μm for elements with ppm concentration. Here we present a means to achieve sub-spot size resolution using inverse methods. We discretize the space sampled in an analysis into pixels and note that the average concentration of the pixels sampled by a spot equals the measured concentration. As multiple overlapping spots sample some of the same pixels, we can combine discrete expressions for each spot as a system of linear equations. Through linear inversion with smoothness constraints we can solve for unknown pixel concentrations. We highlight this approach with two natural examples in which diffusive processes are important: magmatic ascent speeds and (U-Th)/He noble gas thermochronometry. In these examples, accurate results require that the true concentration gradients can be recovered from LA-ICP-MS data. We show that the ability to infer rapid rates of magma ascent is improved from months to weeks and that we are able to interpret previously un-interpretable thermochronometric data.

1. Introduction

Understanding how composition varies across an individual mineral elucidates numerous geological problems, ranging from understanding magmatic systems (e.g. Davidson et al., 2007; Streck, 2008; Bussweiler et al., 2015) to measuring rates of metamorphic processes (e.g. Lasaga and Jiang, 1995; Morgan et al., 2014) to understanding the production and diffusion of noble gases (e.g. Farley et al., 2011; Flowers and Farley, 2012; Fox et al., 2014). Collecting data with high spatial resolution is imperative to maximize the information gleaned from a single crystal analysis. As such, elemental concentrations measured by in situ techniques, such as scanning electron microscopy (SEM), electron microprobe (EMP), secondary ion mass spectrometry (SIMS), transmission electron microscopy (TEM) and laser ablation inductively coupled plasma mass spectrometry (LA-ICP-MS) are typically the methods of choice for such work.

Depending on the method, such analyses, particularly SIMS and TEM work, can be both costly and time-consuming. However, during the last two decades, LA-ICP-MS has advanced significantly to emerge as a cost effective and time-efficient choice, especially when making elemental distribution maps (Ubide et al., 2015, and references therein). Much of this work has focused on increasing the precision and accuracy of the instrumentation to facilitate smaller laser ablation 'spot' sizes. However, the data reduction has received less attention (Paul et al., 2012; Rittner and Müller, 2012; Ortolano et al., 2014; Mouchi et al., 2016), despite the potential to increase resolution of the method by exploiting redundant information.

In some applications measuring zonation, both in terms of the magnitude and the spatial gradients in zonation, is the primary goal of LA-ICP-MS analyses. This is particularly true for the large range of studies involving diffusive processes, in which a diffusant is diffusing through the sample at a specific rate. Therefore, the degree of diffusion and thus the spatial gradient in concentration directly influences the conclusions of the study. For example, Ruprecht and Plank (2013) measured the degree of diffusion of Ni in primitive olivine phenocrysts from primary andesitic melts using LA-ICP-MS to infer the timescale of

---

[*] Corresponding author.
E-mail address: matthew.fox@berkeley.edu (M. Fox).

http://dx.doi.org/10.1016/j.chemgeo.2017.07.001
Received 17 January 2017; Received in revised form 30 June 2017; Accepted 3 July 2017

cooling. In this example, the initial condition is assumed to be a discrete step in Ni concentrations, and diffusion increases the smoothness of zonation boundaries during the months to years magmas take to ascend. However, inaccurately measuring the degree of smoothness can directly influence the inferred timescale of this process. At a different timescale, the spatial distribution of ^{4}He produced from the decay of U and Th in apatites can be measured and related to thermally activated diffusion to infer the timescale of cooling over millions of years (Shuster and Farley, 2004). However, the ^{4}He distribution is also a function of U and Th distributions (Farley et al., 2010), which can be measured by LA-ICP-MS (Farley et al., 2011), and therefore characterizing this distribution is often required to constrain the cooling history.

Previous studies have explored converting LA-ICP-MS data collected across laser spots or line-scans of known size to continuous functions of concentration. However, these approaches do not account for the smearing of information due to the potentially large spot size with respect to concentration gradients. In a 1D case, it is common to fit a function, such as a polynomial or spline, through a plot of distance along transect versus concentration. This approach treats the center of a spot measurement as the independent variable, despite the fact that the spot represents the average of the concentration over a specific horizontal distance. In a 2D case, the grid of concentrations produced via LA-ICP-MS for (U-Th)/He thermochronometry in apatite is processed using an inverse distance weighting (IDW) algorithm (e.g. Farley et al., 2011). This process assigns concentration values to pixels based on the weighted average of surrounding spot measurements, with the weights defined based on the distance between the pixel of interest and the spot measurements. This results in continuous and smooth maps of concentration with pixel sizes on the order of 2 μm × 2 μm. The smoothness of the maps can be controlled with a combination of a power parameter and a radial distance parameter. The radial distance parameter is the main parameter that controls the averaging length-scale (Farley et al., 2011; Tripathy-Lang et al., 2015). Importantly, this approach also treats a spot measurement, which represents the average concentration across an ablated circle, as a single point measurement located at the center of the circle.

Here we present numerical methods to account for this smearing and detect transitions and variations in concentration at a resolution smaller than the spot size. Our approach is based on the fact that an area in a crystal may be sampled by multiple spots or line-scans. In these overlapping areas, individual locations may be associated with multiple spot concentration values. This redundant information can either be averaged to produce smooth maps or exploited to infer sub-spot size concentration variation. We present our inverse approach and highlight its application with the two examples described above: Ni diffusion in olivines to infer the time scale of magma flux and He diffusion in apatite to infer cooling associated with exhumation.

2. Smearing of information due to LA-ICP-MS ablation spot size

Laser ablation measurements can be undertaken using a spot size of known radius. Due to the fact that the spot will measure the average of the ablated material within the spot, discrete changes in elemental concentrations within a spot will be lost. This smearing of information is highlighted in Fig. 1A with a synthetic 1D example. In this synthetic example, measurements have been obtained for three spots that cross a boundary between zone one (Z_1) and zone two (Z_2). The red spot samples only Z_1 and the blue spot samples only Z_2, but the purple spot samples both zones and the concentration measurement is a weighted average of the concentrations from the two zones. The measurements are plotted in 1D in Fig. 1B. Here the dashed lines do not reflect the uncertainty as we assume that the center of the spot is known exactly; these dashed lines represent the distance sampled by each spot and highlight overlapping and thus redundant information. If gradients are inferred from these measurements using simple interpolation methods, the dashed line in Fig. 1C is predicted and the black 'true' concentration profile is not recovered.

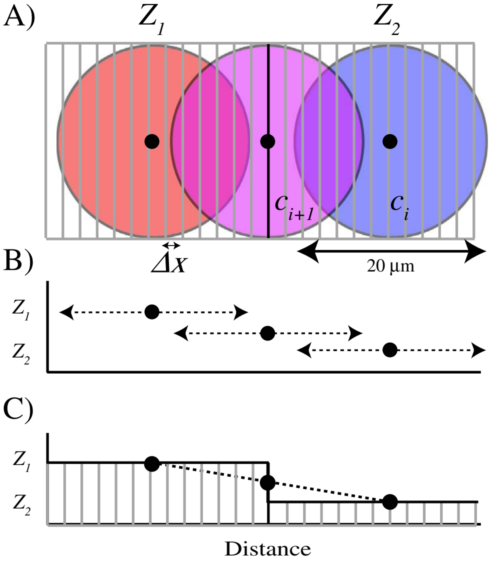

Fig. 1. Synthetic example showing the smearing of boundaries between two zones, Z_1 and Z_2, due to spots sampling Z_1, Z_2, or a combination of both zones. (A) Map view showing the locations of the three spots that sample Z_1, Z_2 and a combination of Z_1 and Z_2. The gray bars show elongate pixels. Three spots are shown sampling two zones separated by the solid black line. (B) Concentration as a function of distance along the profile. The concentrations of Z_1 and Z_2 are labeled on the y-axis. Dashed lines show total distance sampled by a spot along the length of the profile and do not represent uncertainty. (C) The black curve is the true zonation profile and the dashed curve is the inferred profile by linear interpolation between spot measurements. The gray boxes are elongate pixels used for the discretization scheme in the 1D inverse method, where Δx is the width of the pixels. (For interpretation of the references to color in this figure, the reader is referred to the web version of this article.)

The concentration of a spot measured with a laser, s, can be written as the surface integral of the crystal concentration, $c(x,y)$, over the area of the spot, A, divided by the area of the spot:

$$s = \frac{1}{A} \iint_A c(x, y)dxdy. \tag{1}$$

Here we focus on approaches to exploit redundant information obtained from overlapping spots and present a linear inverse approach to reveal the true boundaries in these types of datasets. This approach is based on the assumption that Eq. (1) is a good approximation of the information a spot measurement contains. Therefore, before introducing our approach, we highlight some processes that have the potential to complicate this assumption.

It is important to note that other process also lead to smearing of abrupt changes in concentration. On of the most significant sources of smearing is due to the transient analytical signal of a near-instantaneous input of analyte generated by a single laser pulse. This leads to a predictable increase and then gradual decrease of measured signal (Bleiner and Günther, 2001; Gäckle and Merten, 2005). The bandwidth of this signal is controlled by the wash-in and wash-out characteristics of the ablation cell, the engineered effect of the smoothing manifold and the length of the tubing path to the mass spectrometer. It is possible, therefore, that signals from different parts of the crystals could be mixed and abrupt changes in concentration could be smoothed. Importantly, this is a separate issue that can be accounted for by deconvolving this signal using the linear inverse approach presented by Plotnikov et al. (2002). Alternatively, this issue can be avoided by reducing the scanning rate or firing single shots at a time Cottle et al. (2009). However, the spatial smearing due to overlapping spots remains.

An additional source of smearing is due to the 'ejecta blanket' which is often observed around the ablation site. These ejecta deposits constitute fragmented material formed by sputtering processes and vapor phase condensates from the ablation plume itself. These deposits have the potential to contaminate a new spot measurement. This potential appears to be relatively small for line scans, but can be larger for scans that run very close and parallel to a previous scan (Woodhead et al., 2007). A 'worse case' scenario is presented by Woodhead et al. (2007) in which the ejecta blanket makes up approximately 10% of the ablation signal. This could lead to potential smearing as a spot measurement does not represent the average of the material directly within the spot, as described by Eq. (1). Here, however, we assume that this estimated 10% contamination is unlikely to a major source of smoothing compared to smoothing resulting from overlapping spots.

Finally, we assume that the concentration of a spot on the crystal is constant through an analysis and that multiple measurements at the same location will give the same concentrations. In the case of a 1D profile, a second overlapping spot ablates the material that the first spot ablated a second time. Therefore, there is a chance that this overlapping area may be ablated to twice the depth of the non-overlapping ablated area. We assume, that over this depth interval, the concentration of the crystal is constant. We also make this assumption in the case of 2D maps, in which a specific part of the crystal may be sampled multiple times. We return to the implications of these assumptions in the Discussion.

3. Inverse approach

3.1. 1D linescans

In the case of 1D profiles, we assume that concentrations only vary with distance along the profile. Therefore, we discretize the profile into strips of width Δx (Fig. 1A). A spot will sample each strip, or pixel, as a function of the distance between the edge of the pixel, $x(p)$, and the center of the spot $x(s)$. This is shown in Fig. 2. Here the spot s_i samples a total of m pixels from p_j to p_{j+m}. The area of the spot that samples the example pixel p_e is highlighted in gray. This area is calculated numerically by splitting the coarse strip used for the inversion, p_e, into 100 smaller strips of width Δx_q:

$$area = \sum_{q=0}^{q=100-1} 2^*.\Delta x_q \, ^*\sqrt{r^2 - [(q^*\Delta x_q)+x(p_e)-x(s_i)]^2} \tag{2}$$

where r is the radius of the spot size. Please note, we only calculate this for locations within a spot. In turn, the fraction of the total area of the spot that samples the example pixel is $a_e = area/(area_{tot})$, where $area_{tot}$ is the total area in this discrete form. Each pixel from p_j to p_{j+m} will represent a slightly different fraction of the i^{th} spot, a_j^i.

This allows a discrete version of Eq. (1) to be written in terms of elongate pixels:

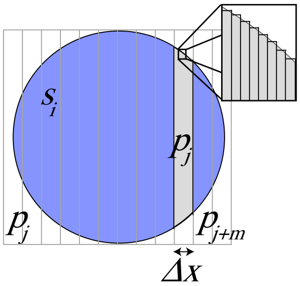

Fig. 2. Discretization of the i^{th} circular spot into elongate pixels. Pixels further from the center of the spot cover a smaller fraction of the total area of the spot than pixels close to the center. The spot samples a total of m pixels from p_j to p_{j+m}. The area sampled of a single example pixel, p_e, is shown by the gray area. The inset shows how a single pixel is sub-divided into smaller pixels to accurately calculate the area of the pixel that is sampled by a spot.

$$s_i = \sum_{j=j_1}^{j_1+m} p_j * a_j^i \tag{3}$$

where j_1 is the first pixel that the spot samples. We can write a separate discrete expression for each spot in a single 1D line scan, accounting for the fact that they sample the same pixels to different degrees. For example, consider a 1D dataset made up of three spots with large pixel sizes such that each spot samples only three pixels. The first spot samples the first three pixels, the second spot samples p_3 to p_5 and the third spot samples p_5 to p_7. This scenario can be written as three separate summations and described as a series of vector products:

$$\begin{bmatrix} a_1^1 & a_2^1 & a_3^1 & . & . & . & . \\ . & . & a_3^2 & a_4^2 & a_5^2 & . & . \\ . & . & . & . & a_5^3 & a_6^3 & a_7^3 \end{bmatrix} \begin{bmatrix} p_1 \\ p_2 \\ p_3 \\ p_4 \\ p_5 \\ p_6 \\ p_7 \end{bmatrix} = \begin{bmatrix} s_1 \\ s_2 \\ s_3 \end{bmatrix} \tag{4}$$

In this example, it can be seen that the pixels p_3 and p_5 are both sampled by two spots, because there are two entries in the third and fifth columns of the matrix. This can be combined in matrix form:

$$\mathbf{Ap} = \mathbf{s} \tag{5}$$

where $\mathbf{p}$ is a vector of length equal to the total number of pixels sampled in a 1D line scan (n_p), $\mathbf{s}$ is a vector of length equal to the total number of spots in the line scan (n_s), and $\mathbf{A}$ is a matrix of size n_p by n_s and contains fractions of areas calculated using Eq. (2) and each row of $\mathbf{A}$ sums to the area of the spot.

The problem is potentially mixed determined in that some pixels will be sampled by many spots, but some may not be sampled at all due to problems with data collection. There are many reasons why part of a line scan may not be usable, due to human errors or instrument errors. In reality, the problem of pixels that are not sampled will more likely be encountered in the 2D case, discussed below. Therefore, to solve these independent equations, we utilize the a priori knowledge that concentration is likely to be correlated in space. This is achieved by incorporating smoothness constraints directly into Eq. (5). In particular, we use Occam's inversion (Constable et al., 1987) in which we seek the smoothest model that is consistent with the data where smoothness, or roughness, is quantified using a discrete Laplacian (Constable et al., 1987). This is a form of Tikhonov regularization and this type of inversion is used extensively within the Earth Sciences from 3D seismic tomography (e.g. Sambridge, 1990), to heat flow problems (e.g. Gallagher and Sambridge, 1992), and from slip distributions on fault planes during earthquakes (e.g. Segall and Harris, 1987) to inferring uplift rates from river profiles (e.g. Goren et al., 2014). In all these approaches there is no definitive way to pick the degree of regularization and models are chosen based on balancing the degree of data fit with properties of the model. This is commonly achieved using the L-curve, in which data fit is plotted against model smoothness for models obtained with different regularization and the optimal model is chosen close to the origin (e.g. Hansen, 1992). However, additional datasets or prior information can also be used when choosing models. For example, if zonation has been observed in a crystal using a different approach (e.g., with EMP or cathodoluminescence), these data should be used to guide model selection.

This constraint is imposed by adding to additional rows to Eq. (5). Each row corresponds to a single pixel and describes a discrete negative 1D Laplacian of the form:

$$\alpha \nabla^2 p_j = 2^* p_j - p_{j-1} - p_{j+1}, \tag{6}$$

where α accounts for the grid spacing and weighting as described below. If the concentration of the central pixel and the two adjacent pixels are the same, this row is equal to zero. In addition, if the gradient in concentration is constant, this row is equal to zero. However, as the degree of concentration variations increases, this value also increases. At boundary pixels, only the one neighboring pixel is included (i.e., $\alpha\nabla^2 p_1 = p_1 - p_2$). Eq. (6) can be written for each pixel and combined in matrix form, $\alpha\nabla^2\mathbf{p}$. When this matrix-vector product is equal to zero, the concentration is either constant everywhere or defines a straight line. Therefore, the smoothness constraints that are minimized in the inversion can be written as:

$$\alpha\nabla^2\mathbf{p} = \mathbf{0}, \tag{7}$$

where $\mathbf{0}$ is a vector of length n_p. Combining this expression with Eq. (11) gives

$$\begin{pmatrix} \mathbf{A} \\ \cdots \\ \alpha\nabla^2 \end{pmatrix}\mathbf{p} = \begin{pmatrix} \mathbf{s} \\ \cdots \\ \mathbf{0} \end{pmatrix}. \tag{8}$$

Solving this system of equations in a least squares approach to minimize the misfit, ϕ, provides pixel concentrations that can be smooth in space and fit the data:

$$\phi = \|\mathbf{Ap}-\mathbf{s}\|^2 + \alpha^2\ \|\nabla^2\mathbf{p}-\mathbf{0}\|^2. \tag{9}$$

If α is small, the expression on the right is small and the degree of roughness has a small effect on ϕ. The solution will fit the data well, but this solution will be sensitive to noise and potentially unrealistic. In contrast, if α is large, a smooth solution will be found, which may not fit the data well. This trade-off must be explored when choosing a value for α and we recommend a systematic approach to determine a preferred value for α.

3.2. 2D concentration maps

In the 2D case we discretize Eq. (1) into pixels of size $\Delta x\Delta y$ (Fig. 3). Therefore, the concentration of the i^{th} spot can be written as a function of the set of pixels that the spot samples, M_i:

$$s_i = \frac{1}{S_i}\sum_{j\in M_i} f_j^i p_j \quad * \quad \Delta x\Delta y \tag{10}$$

where s_i, is the average concentration within the i^{th} spot in an analysis, p_j is the average concentration within a pixel located within the area defined by the spot center and radius of the spot. Finally f_j^i is the fraction of a pixel that is sampled by the spot, for example, if the pixel is totally within the spot, $f_j^i = 1$. As above, f_j^i this is calculated numerically sub-dividing each pixel into smaller areas. Each pixel is defined using a 2D grid and therefore, p_j actually indicates the coordinates of a specific pixel $p_{l,k}$. Here S_i is the total size of the spot in this discrete form, i.e., $\sum_{j\in M_i} f_j^i a_j \Delta x\Delta y$.

As above, since overlapping spots will sample the same pixels, expressions for each spot as a function of pixels can be combined in matrix form:

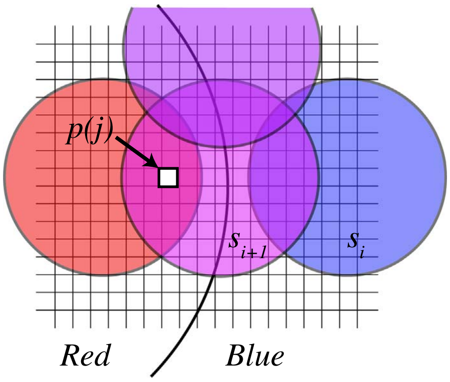

Fig. 3. Synthetic example showing the discretization of space in 2D. Note that some pixels will be sampled by multiple spots but others will only be sampled by one spot. The concentration of a given spot is the average of the concentrations of the pixels it samples.

$$\mathbf{Ap} = \mathbf{s} \tag{11}$$

where $\mathbf{A}$ is a matrix in which row i contains fractions of areas at columns that denote specific locations in space which are within the i^{th} spot. Therefore, $\mathbf{A}$ has n_s rows, where n_s is the number of spots measured and has n_p columns, where n_p is the number of pixels used to discretize the total area that was analyzed.

In the 2D case, 2D smoothness constraints are imposed using a discrete negative 2D Laplacian of the form:

$$\lambda\nabla^2 p_{l,m} = 4{*}p_{l,m} - p_{l+1,m} - p_{l-1,m} - p_{l,m+1} - p_{l,m-1}, \tag{12}$$

where λ accounts for the grid spacing and weighting as described below. If the concentration of the central pixel and the four adjacent pixels are the same, this row is equal to zero. However, as the degree of concentration variations increases, this value also increases. At boundary pixels and corner pixels, only surrounding nodes are combined (i.e., $\lambda\nabla^2 p_{1,1} = (2 * p_{1,1} - p_{2,1} - p_{1,2})$. Eq. (12) can be written for each pixel and these rows are set equal to zero and combined in matrix form and combined with the forward model expressions, as above. The resulting equation can be solved to determine spatial variations in concentration with the same trade-off between model smoothness and fit to the data.

3.3. Data uncertainty

Finally, data uncertainty can be accounted for so that precise data are given more weight than imprecise data in both the 1D and 2D case. This can be achieved by defining a data weighting matrix, W_d of size $n_s \times n_s$, with entries of one over measured uncertainties along the main diagonal and zeros elsewhere, such that $W_d(i,i) = 1/\sigma_i$ (Tarantola, 2005). This is combined with Eq. (8):

$$\begin{pmatrix} \mathbf{W_d A} \\ \cdots \\ \lambda\nabla^2 \end{pmatrix}\mathbf{p} = \begin{pmatrix} \mathbf{W_d s} \\ \cdots \\ \mathbf{0} \end{pmatrix}. \tag{13}$$

In some cases, it will be possible to treat the data as stochastic variables characterized by a mean value and a full data covariance matrix, $\mathbf{C_D}$ (Vermeesch, 2015; McLean et al., 2016), where $\mathbf{C_D}$ is equivalent to $\mathbf{W_d}^{-0.5}$. Modifying Eq. (13) to include the full covariance matrix therefore requires replacing W_d with $\mathbf{C_D}^{-0.5}$. However, if making maps of concentration is the primary goal of the analysis, it is not clear whether including measurement uncertainty is appropriate and we return to this point below.

Eq. (8) or Eq. (13) can be solved with iterative methods and additional constraints can be incorporated, such that concentration is positive. Here, we use the MATLAB function `lsqlin` to solve these systems of equations and the required code is provided in the Supplementary Material.

3.4. Model uncertainty

Estimating uncertainties associated with the calculated pixel concentrations is challenging. This is largely because our solutions to Eqs. (5) and (11) are non-unique. Regularization is required to infer pixel concentrations and thus the choice of the damping parameters influences the results and any estimates of uncertainty. Furthermore, the choice of the damping parameters depends on the pixel sizes used in the analysis.

It is also important to note that interpreting model uncertainty can be challenging because model parameters will be correlated. In many cases, the uncertainty is used as a means to assess the 'quality' of the solution at a specific pixel. However, in some instances the zonation information will be required in a forward model or as data that must be explained with a model. In these cases, the correlations amongst model parameters should be accounted for. Therefore, a single zonation model can be defined by a mean concentration value for each pixel and a model covariance matrix. A single realization of the zonation model would account for the model correlations. For example, if concentration in one pixel sampled by a spot is increased with respect to the mean concentration, concentrations elsewhere will decrease to ensure that the average concentration within the spot remains constant. Importantly, the estimated concentrations given by the mean concentration in each pixel plus the estimated uncertainty at each pixel will not be a true realization of the zonation model, because model uncertainties are not accounted for. We return to this point in the 2D example below.

Below we suggest two ways to estimate model uncertainty using the bootstrap method and linear error propagation. But first we provide an alternative approach to choose the value of damping parameters.

3.4.1. *The smoothest model that fits the data*

If the errors are accurately known, a damping parameter can be chosen based on the requirement that the model fits the data to within error. The procedure for this approach is to run several inversions for smaller and smaller values of the damping parameter, stopping this process once the data are fit to within error. If there was no regularization, this would be equivalent to stopping once the reduced χ^2 value is equal to one, with the number of degrees of freedom equal to the number of spots minus the number of pixels, $df = n_s - n_p$. However, in regularized inversions the fitted parameters are linked as a function of the damping. For example, for a very large value of α, the results of a 1D inversion will approach a straight line, which can be described with only two parameters. In contrast, when α is very small, the number of fitted parameters will approach the total number of pixels n_p. As recently shown by McLean et al. (2016) for the treatment of LA-ICP-MS data, the Welch-Satterthwaite formula provides a means to calculate number of degrees of freedom despite damping:

$$df = trace(\mathbf{H}^t\mathbf{H})/trace(\mathbf{H}^t\mathbf{H}\mathbf{H}^t\mathbf{H}), \tag{14}$$

where $\mathbf{H}$ is commonly termed to the hat matrix and is given by:

$$\mathbf{H} = \mathbf{A}_\nabla(\mathbf{A}_\nabla^t\mathbf{A}_\nabla)^{-1}\mathbf{A}_\nabla \tag{15}$$

where $\mathbf{A}_\nabla$ is the simplification:

$$\mathbf{A}_\nabla = \begin{pmatrix} \mathbf{W_d A} \\ \cdots \\ \alpha\nabla^2 \end{pmatrix}. \tag{16}$$

For more information on utilizing the Welch-Satterthwaite formula to select damping parameters please refer to McLean et al. (2016).

The approach outlined above to infer model uncertainty requires that the total data uncertainty budget (i.e., measurement uncertainty, overdispersion and geological uncertainty) is accurately known. It is important to note, however, that there are two general factors that might make using analytical measurement uncertainties obtained from LA-ICP-MS data challenging. First, measurements of higher concentration areas in a crystal are expected to yield smaller measurement uncertainty compared to low concentration areas. This is a result of the increased signal intensity in these areas. However, it is unclear whether these areas should dominate the results of an analysis. This is the case whether our linear inverse method is used or whether results of diffusion models are fit directly to the data. Second LA-ICP-MS data are often overdispersed because measurement uncertainties typically underestimate total uncertainty budgets, and because of subtle changes in plasma conditions during the run despite accounting for plasma drift (Fox and Ickert, 2015; McLean et al., 2016). An approach to account for this is to add an overdispersion term directly to the measurement uncertainties (McLean et al., 2016). However, it is challenging to directly estimate overdispersion in an ill-posed inverse problem and this is often a subjective choice left to the user. Furthermore, the matrix $\mathbf{H}$ is often a dense matrix that can be challenging to store and calculate on laptop computers.

For these reasons, we advise that the choice of these damping parameters be dependent on results of the L-curve and achieving results that are reasonable. In practical terms this means choosing a model that fits the data to some degree but is also informed by prior knowledge. As an example, if the calculated zonation does not resemble expected zonation profiles, then the damping parameter may not be suitable. Expected zonation may be that concentration values are similar at similar distances from the edge of a crystal, reflecting diffusive processes or successive stages of crystal growth.

3.4.2. *Model uncertainty through bootstrapping*

Once a suitable damping parameter has been identified, either through the L-curve method or using a modified reduced χ^2, model uncertainties can be calculated using the bootstrap method of resampling residuals with replacement (Efron, 1979). This method proceeds as follows: 1) predict pixel concentrations, $\mathbf{p}$, and calculate residuals between measured spot concentrations and model predicted spot concentrations, ε; 2) add a randomly drawn residual to each spot measurement to generate a new synthetic dataset of spot measurements set, $\hat{\mathbf{s}}$, e.g. $\hat{s}_i = s_i + \varepsilon_r$, where r is a random index; 3) predict pixel concentrations using $\hat{\mathbf{s}}$, $\hat{\mathbf{p}}$; 4) repeat steps 2 to 4 many times.

The resulting set of inferred pixel concentrations can be analyzed to infer error bounds on the estimate. For example, for any pixel location, one standard deviation can be calculated by ranking all inferred concentration values for that pixel and finding values that are 34% of the total number of values either side of the mean value. This approach has the advantage in that the model errors are not assumed to be Gaussian and symmetrical and therefore negative concentrations are never predicted.

3.4.3. *Model uncertainty through error propagation*

An alternative to bootstrapping, is to calculate model uncertainty directly by propagating data uncertainty. It is equivalent to write Eq. (13) with the data covariance matrix included for completeness as (Tarantola, 2005; Snieder and Trampert, 1999):

$$(\mathbf{A^t C_D^{-1} A} + (\alpha^2\nabla^2)^2)\mathbf{p} = \mathbf{A^t C_D^{-1} s} \tag{17}$$

In this form, $\mathbf{p}$ can be calculated using the explicit formula:

$$\mathbf{p} = (\mathbf{A^t C_D^{-1} A} + (\alpha^2\nabla^2)^2)^{-1}\mathbf{A^t C_D^{-1} s}. \tag{18}$$

If we make the simplification:

$$\mathbf{p} = \mathbf{Ks} \tag{19}$$

where $\mathbf{K} = (\mathbf{A^t C_D^{-1} A} + (\alpha^2\nabla^2)^2)^{-1}\mathbf{A^t C_D^{-1}}$, we can propagate data covariance directly to model covariance (Menke, 2012),

$$\mathbf{P}_\epsilon = \mathbf{K C_D K}^t \tag{20}$$

and the uncertainty on each model parameter is the square-root of the corresponding diagonal entry in the $n_p \times n_p\mathbf{P}_\epsilon$ matrix. This approach has the disadvantage in that model errors are assumed to be Gaussian and symmetrical, which is likely to be a problem as concentrations approach zero. It can also be computationally expensive to calculate $\mathbf{P}_\epsilon$. An advantage, however, of this method is that model covariance is calculated and thus it is possible to draw realizations of the zonation model. One way to generate a model realization, $\mathbf{p_r}$, is to perturb the mean pixel concentrations, $\mathbf{p}$:

$$\mathbf{p_r} = \mathbf{p} + \mathbf{Fz} \tag{21}$$

where $\mathbf{z}$ is a vector of independent, standard, normally distributed (zero expectation, unit variance) random numbers. $\mathbf{F}$ is a matrix such that,

$$\mathbf{FF}^t = \mathbf{P}_\epsilon \tag{22}$$

and can be obtained using the Cholesky decomposition (Devroye, 1986). This is achieved using the Matlab command $p_r =$ `mvnrnd` $(\mathbf{p}, P_\epsilon)$.

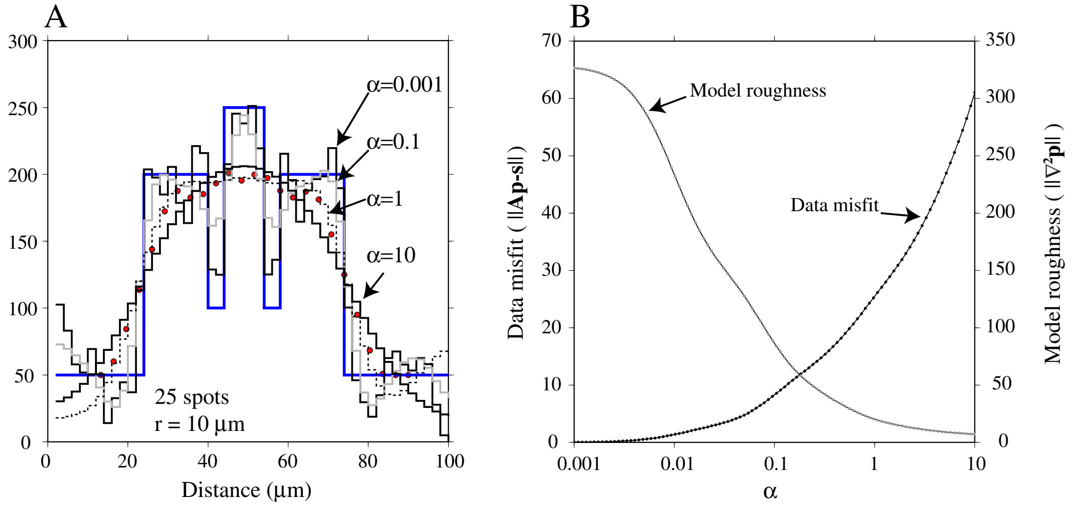

Fig. 4. 1D synthetic example. (A) The blue line is the 'true' concentration profile that we sample with a spot of known radius. This concentration is sampled with 25 spots with a radius of 10 µm to produce the red data points, which do not follow the true concentration profile due to averaging within each spot. Solving Eq. (8) with a range of values for *α* results in the dashed curves. In general, our inverse approach provides a means to recover the true profile. (B) The trade-off between model roughness and data misfit as a function of *α*. At small values of *α* the data reproduced but the model may be overly complex with artefacts introduced by non-unique solutions to Eq. (8). At large ? values the solution is smooth and is equivalent to linear interpolation between the data points. Each black point represents a separate inversion result. (For interpretation of the references to color in this figure legend, the reader is referred to the web version of this article.)

4. Results

4.1. Example 1: 1D synthetic example and parameter exploration

We test this approach using a complex synthetic example. In this example, the blue line is the 'true' concentration profile, Fig. 4A. This true profile is sampled with a synthetic laser with a known spot size and a grid size of 2 µm and use Eqs. (2) and (3) are used to predict synthetic data. These data do not follow the true concentration profile due to averaging within each spot, Fig. 4A. Furthermore, if a simple interpolation scheme was used to infer the concentration profile, many of the characteristics of the profile would be lost.

Solving Eq. (8) with a range of values for *α* allows the utility of the inverse approach to be tested. For a small value of *α* of 0.001, a concentration profile is recovered that follows the main features of the true profile and captures the low concentration values either side of the central peak, Fig. 4A. However, there are also many artefacts introduced. For example, high values are inferred on the shoulders of some of the abrupt concentration changes leading to increased roughness. With larger values of *α* of 0.1, gray curve, we recover a smoother concentration profile. However, some of the extreme values are less well recovered. In particular, the low concentration values on either side of the central peak are not as low as the previous example. With further increases in *α*, smoother profiles are recovered and the underlying true profile becomes unrecognizable.

The trade-off between model smoothness and data misfit as a function of *α*, described in Eq. (9), can be explored in more detail, Fig. 4B. Here we discuss roughness as opposed to smoothness, simply because the numerical value of ($\|\mathbf{p}\|$) increases with increasing roughness. For small values of *α*, the total misfit, ϕ is dominated by data misfit ($\|\mathbf{A}\ \mathbf{p}\ -\mathbf{s}\|$). Therefore, data misfit values are low and model roughness values ($\|\mathbf{p}\|$) are large. With increased *α*, the influence of model roughness on total misfit increases and data misfit increases. In this respect, there is a trade-off between model roughness and data misfit. This trade-off between model smoothness and data misfit must be explored systematically, and other available information or constraints should be used to help select an appropriate value of *α*. This is important when analyzing real data as noise in datasets can be problematic with small values of *α* because the inversion will attempt to fit anomalous data points at the expense of model smoothness. We return to the problem associated with noise in the Discussion.

4.2. Example 2: 1D example applied to magma flux

We next test this approach using a 1D published example. Ruprecht and Plank (2013) measure nickel zonation in primitive olivine crystals using LA-ICP-MS. These zonation profiles contain information about the temperature-time history of these crystals, from which we can make inferences about the rate of magma fluxes from the mantle, based on the assumption that the nickel diffuses within the crystal as a function of time and temperature (Costa et al., 2003). Using the data and a model for nickel diffusion in olivine, Ruprecht and Plank (2013) inferred that within the Iraz volcano, Costa Rica, magmas ascend from their source in the mantle through about 35 km of crust in months to years. In this example, the smoothness of the zonation profile directly determines the inferred timescale of magma ascent. The authors do point out that both the amplitude and the wavelength of Ni variations are almost identical when measured by LA-ICP-MS and electron microprobe techniques, suggesting that LA-ICP-MS profiles resolve the true gradual variations. This highlights that the inevitable smearing of sharp step variations is insignificant for their data because the variations are actually diffuse. Our analysis of only the LA-ICP-MS data also support these gradual variations and show that the timescales inferred by Ruprecht and Plank (2013) are robust with respect to smearing. We also perform a resolution test to show when smearing will have an appreciable effect on inferred time scales.

We explore the potential for smearing in their data and assess the effects of this on the inferred timescales of magma ascent. Further, we show that the degree of smoothness that they mapped in this case will not be influenced by the smearing due to large spot sizes. Fig. 5A shows the measured concentrations (red circles) and the recovered zonation gradient (black stepped curve). No measurement uncertainties were reported for this dataset (Ruprecht and Plank, 2013) and thus we recover zonation gradients using Eq. (8). The recovered zonation profile passes through the data and would be identical to a curve obtained by smoothly interpolating between the data. The blue curves show predicted concentration profiles following diffusion of Ni at 1100 °C for 5 years and 1 month to highlight the diffusive process. These profiles are calculated using analytical solutions to the diffusion equation in an infinite medium with fixed boundary conditions with a diffusivity of

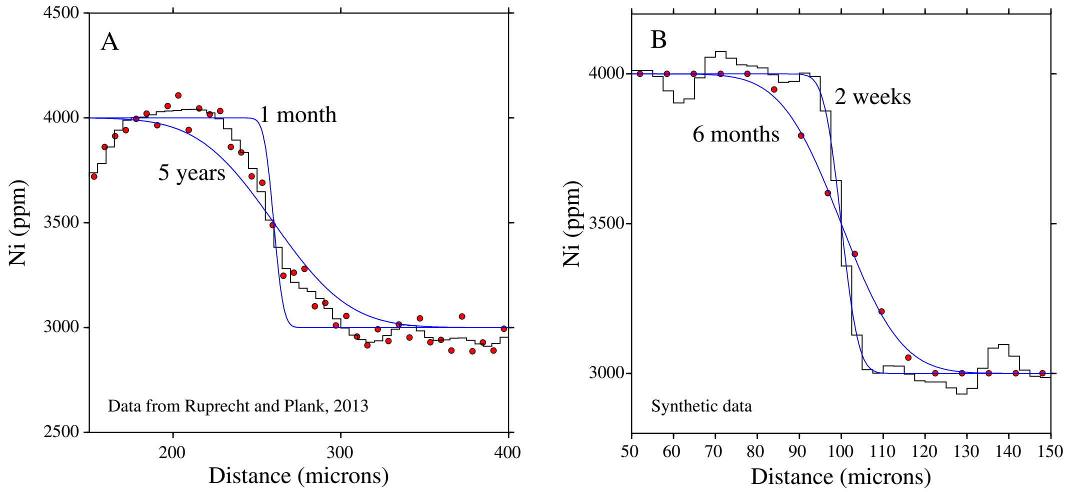

Fig. 5. 1D example using LA-ICP-MS data from primitive olivines reported by Ruprecht and Plank (2013). (A) The center of spots of measured concentrations are shown in red circles, and the recovered zonation gradient is shown as the black stepped curve and is calculated using Eq. (8). This curve passes through the data and is equivalent to linear interpolation between the data points. The blue curves show predicted concentration profiles following diffusion of Ni at 1100 °C for 5 years and 1 month from an initial condition that is a discrete step. (B) Resolution analysis for this method highlighting the decreased resolution due to spot smearing. We assumed a spot size of 20 μm and produced synthetic data, red circles, for the initial condition prior to any diffusion, with a discontinuous drop in Ni concentration from 4000 ppm to 3000 ppm at 100 μm along a line-scan. The recovered zonation is shown as the black stepped curve. The blue curves show that the shortest period of time that recoverable for interpolating between data points is approximately 6 months, whereas if this smearing is accounted, a timescale of 2 weeks is resolvable. (For interpretation of the references to color in this figure legend, the reader is referred to the web version of this article.)

4×10^{-18} m^2 s^{-1} (Costa et al., 2003).

We further explore the potential of our method to resolve discrete boundaries by asking the question: how does our inversion scheme change the temporal resolution of this approach? For this synthetic experiment we assumed a spot size of 20 μm diameter and produced synthetic data for the initial condition prior to any diffusion, with a discontinuous drop in Ni concentration from 4000 ppm to 3000 ppm at 100 μm along a line-scan.

The predicted data are shown in Fig. 5B as red circles and no errors are added to the data. The recovered zonation is shown as the black stepped curve. This calculation demonstrates that the smearing effect of LA-ICP-MS data collection can result in the appearance of diffusive distributions from a concentration discontinuity. Thus, if interpreted as having resulted from diffusive mobility of Ni, this artefact results in an overestimation of the diffusive timescale, for a given diffusivity. The blue curves show that the shortest period of time that is predicted for linear interpolating between data points is approximately 6 months, whereas this simulated discontinuous distribution occurred over an infinitesimal timescale. However, if an inverse method is used to account for smearing, the temporal resolution can be reduced from 6 months to 2 weeks. Note that this time interval is still 2 weeks longer than the true instantaneous value and this represents the error introduced by damping. As the damping is decreased however, results become more sensitive to noise in the dataset. We provide a Matlab script to further explore the sensitivity of the results to the damping parameters and noise in the Supplementary Material.

4.3. Example 3: 2D Yosemite Valley thermochronometry

We now test our inversion scheme using an example from Yosemite Valley. Here rocks at the surface cooled due to the processes of erosion, and therefore this cooling history provides a direct record of landscape evolution (Shuster and Farley, 2004; Shuster et al., 2005). By measuring the stepwise release of radiogenic ^{4}He with respect to artificially proton-induced ^{3}He during heating of individual crystals (Shuster and Farley, 2004), the spatial distribution of ^{4}He can be measured. This distribution is a function of: 1) the thermal history, as ^{4}He is lost through diffusion; and 2), the spatial distribution of U and Th, as this determines where ^{4}He is produced. The long stopping distances of α particles modifies this distribution, however this can be accounted for (Farley et al., 1996). In some cases, the zonation of U and Th represents a primary control on the ^{4}He/^{3}He release spectrum (Fox et al., 2014), making inferring time-temperature information from ^{4}He/^{3}He data challenging. By combining ^{4}He/^{3}He stepwise degassing experiments with a measure of the spatial variations in ^{4}He production rate, the accuracy of the inferred time-temperature paths increases (Flowers and

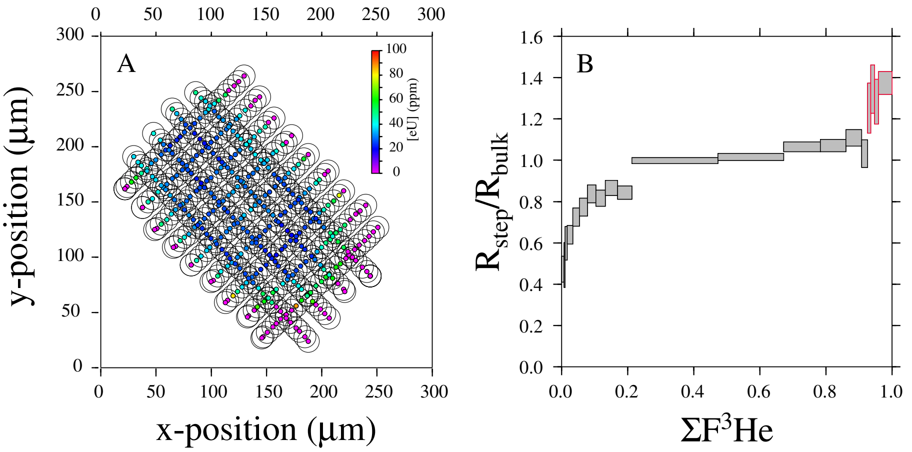

Fig. 6. ^{4}He/^{3}He thermochronometric data from Yosemite Valley. (A) eU concentration ([U] + 0.235[Th]) measured by LA-ICP-MS data from same crystal. The center of each spot is plotted along with a radius that corresponds to the spot size. (B) The x-axis is cumulative release fraction of proton-induced ^{3}He; y-axis is the R_{step}/R_{bulk} value (where R is the ratio of ^{4}He/^{3}He measured in a single step and R_{bulk} is the ratio of all steps summed). The steps highlighted with the red outline are considered outliers. (For interpretation of the references to color in this figure legend, the reader is referred to the web version of this article.)

Farley, 2012; Fox and Shuster, 2014).

We collected ^{4}He/^{3}He thermochronometric data (Fig. 6B) and LA-ICP-MS data (Fig. 6A) from a crystal from Yosemite Valley National Park located along Tioga Road, north of, and above, the main valley near the head of Tamarack Creek (37.782°, −119.745°). Milligram quantities of apatite crystals were irradiated with 1.0×10^{16} p/cm^2 with incident energy of 220 MeV over ~5 h at the Francis H. Burr Proton Therapy Center at the Massachusetts General Hospital (Shuster and Farley, 2004). Following irradiation, a single apatite crystal was placed into a Pt-Ir packet and sequentially degassed at controlled temperatures using a pyrometer-controlled 70 W diode laser in the Noble Gas Thermochronometry Lab of Berkeley Geochronology Center following methods described in Tremblay et al. (2015). After degassing, the crystal was recovered and mounted in epoxy, and polished to expose an internal plane perpendicular to the shortest axis of the crystal at roughly half the depth. This depth was estimated based on visual inspection with an optical microscope. All isotope measurements were obtained using a Photon Machines Analyte G2 laser attached to a Thermo Scientific Neptune Plus ICP-MS. No smoothing manifold was used. The laser recorded precise x-y locations at 2-second increments along line-scans executing at a rate of approximately 1 μm/s. Laser operation settings were as follows: a rep rate of 5 Hz, a spot diameter of 20 μmm, a 20% laser energy output corresponding to a fluence of 1.36 J/cm^2. Laser ablation line-scans began and ended in epoxy, thus fully traversing the crystal and the crystal boundaries. This boundary was defined by tracking the rise of ^{43}Ca. ^{238}U and ^{232}Th was calibrated using a 100 μm long analysis in Durango apatite, using ^{43}Ca as the internal standard. All Durango apatite calibrations were run at equivalent laser settings to unknowns and analyzed immediately prior and subsequent to the measurement of a single crystal. The Durango standard was used to estimate the error associated with the U and Th concentration measurements for the unknowns. The typical variability is ~9.8% at the 1 sigma level and no trends in concentration across the Durango standard were observed suggesting that this error represents random errors and not systematic zonation that may be expected across large shards of Durango (Boyce and Hodges, 2005). No errors on individual concentration measurements were measured as the typical variability of our standard dominates that error and therefore we assume uniform measurement uncertainty of 9.8% of the average concentration. A table with LA-ICP-MS parameters is included in the Supplementary Material.

During a continuous line-scan, measurements of ^{238}U, ^{232}Th, and ^{43}Ca were cycled through, taking approximately 6.3 s, which translates into 6.3 μm for one complete cycle at a laser line-scan speed of 1 μm/s. There is a 2.8 second delay between measuring ^{238}U and ^{232}Th and ^{43}Ca; therefore the ^{43}Ca measurement is taken at the approximate midpoint of each cycle (3.2 s), which translates to the physical midpoint of the approximately 6.3 μm scan. Because of this delay, linear interpolation between preceding and succeeding blank-corrected ^{238}U and ^{232}Th measurements was used to obtain the best estimate of these measurements at the time and location of the ^{43}Ca measurement. The result is a spatially referenced grid of ^{238}U and ^{232}Th measurements (Fig. 6A). See Tremblay et al. (2015) for further details related to data collection.

We use our inverse method to convert the spot measurements to maps of ^{238}U and ^{232}Th. Several zonation patterns were calculated using a range of different values controlling the model smoothness. Because the total measurement uncertainty budget is not fully quantified, we constructed an L-curve for a range of solutions with different λ values (Fig. 7A). Here model roughness is calculated $\|\nabla^2 \mathbf{p}\|$ and data misfit is $\sqrt{\sum_{i=1}^{n_s} \frac{r_i^2}{\sigma_i^2}}$, where r_i is the residual between the measured and predicted i^{th} spot concentration and σ_i is the observed measurement uncertainty. The results of the L-curve show that with small values of λ and high model roughness, data misfit is low. Conversely, with low model roughness data misfit is high. Preferred solutions will be close to the corner of the L-curve. Two examples are shown with a small amount of damping and a large amount of damping (Fig. 7B). As with the 1D synthetic example, small values of λ lead to noisy results and a 'lumpy' map of concentration in which high eU zones are small and isolated. In contrast, with high values of λ the results are overly smooth and features of the zonation are lost. We select a solution from the suite of recovered models with an λ value of 0.175 that is both close to the corner of the L-curve and is reasonable given our prior knowledge of how crystals grow over time (Fig. 8A). Uncertainty associated with this particular solution has been achieved by bootstrapping with 1000 samples, as discussed above (Fig. 8B). It is important to note that here we use the uncertainty as a means to highlight where the model is well constrained by the data. We also provide a means to visualize model covariances through propagation of errors by realizing 20 zonation models (Supplementary Materials). These models account for the model covariance structure and highlight dominant features of our recovered zonation model that are robust. Because of the similarities between the model realizations, we do not propagate this uncertainty below.

We also use the conventional IDW interpolation method to convert the spot measurements to maps of ^{238}U and ^{232}Th, and convert the 2D maps into 1D spherically symmetric zonation models following the method outlined in Farley et al. (2011) (Fig. 9A). Unlike our method in which the smearing of crystal boundaries is accounted for, the IDW method requires that only spots fully on the crystal be included in the analysis. Therefore, cycles where the beam includes any epoxy signal are removed for the IDW method. This introduces a level of subjectivity as spots partially in epoxy will record lower concentrations than spots fully in the crystal despite constant concentration within the crystal. This apparent increase in concentration is hard to distinguish from true zonation. Therefore we must decide when a spot is fully within the crystal based on calcium signal strength. Importantly this concentration map is very different from the recovered zonation model, and the realizations of the zonation model presented in the Supplementary Material.

Due to the relatively simple recovered zonation pattern, 3D methods are not required (Fox et al., 2014), thus allowing us to use 1D methods to solve the He diffusion problem. Therefore, we use the approach of Farley et al. (2011) to convert both the preferred zonation map obtained through our linear inversion method and the map obtained through the IDW method into 1D spherically symmetric zonation models (Fig. 9B), which can be used in 1D numerical models of He diffusion.

A random search algorithm is then used to find time-temperature paths that are consistent with the observed release spectra for the IDW map and the selected linear inversion map (Fox and Shuster, 2014) (Fig. 10). All paths start at 150 °C and 90 Ma, which is approximately the crystallization age, and reach the surface at 0 °C at the present day. We test 5000 random time-temperature paths for both zonation models and show the best 500 time temperature paths for each zonation model. Clearly, we are able to explain more of the data by accounting for smearing due to the laser spot size (Fig. 10). Furthermore, we are able to recover a thermal history from data which, without accounting for the complex distribution of the parent isotopes, was previously unexplainable. In some cases the differences between the recovered time-temperature paths will be crucial for the interpretation of the data and this is discussed below.

5. Discussion

Our approach is designed to exploit redundant information to infer spatial variations in concentration. In other approaches, this redundant information has been used to average concentrations at individual locations, thereby reducing the influence of signal noise. In this respect, our inverse approach accentuates noise and is sensitive to outliers. Therefore, any outliers must be identified prior to producing maps of concentration and not included in the inversion. This requires that the

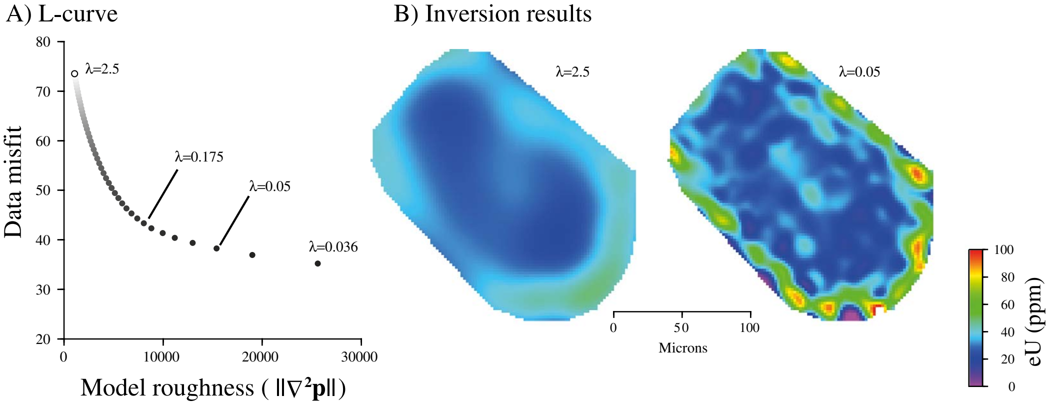

Fig. 7. Results of the proposed inverse method using the data shown in Fig. 6. (A) L-curve showing how changes in the value of λ which controls the smoothness of the recovered zonation map and also fit to the data. Each point on the curve is the result of an inversion for a different value of λ where λ varies from 2.5 to 0.036. (B) Maps of concentration for two example inversion results. A large value of λ results in very smooth models but the data is poorly reproduced. In contrast, results with small values of λ fit the data well but leads to a lumpy solution that does not resemble expected zonation.

data are carefully inspected for any outliers prior to any analysis of the data. It is important to note, however, that noise can be reduced by collecting more data. For example, in the case of 1D line-scans, multiple parallel lines may capture the same zonation profile if they are all perpendicular a concentration boundary inside a grain. However, unless inverse methods are used, the true zonation profile may not be recoverable regardless of how many line-scans are repeated. Instead, these line-scans can be averaged to reduce noise and then the average profile could be used in the inverse scheme.

We assume that concentration does not vary with depth at the scale of the depth of a typical laser spot. These spot sizes are typically 20 μm across, but usually less than approximately 10 μm deep. Therefore, we assume that material from the top of the spot will be identical to material from the bottom of the spot. This is important because it means that we assume that if we revisit the same location on the crystal multiple times, the true concentration value at that location remains unchanged. In reality, zonation concentrations may vary as a function of depth. In the future, we could account for this potential complication by collecting data from different sections through the crystal and using these different sections to estimate how rapidly concentration varies with depth. We could also collect a combination of spot measurements and depth profiles. Ultimately, we could design experiments to collect data in three dimensions and extend our inverse scheme into the third dimension.

The approach presented here will not artificially increase zonation gradients. This is highlighted in Fig. 5A. Here the true gradients in Ni concentration are not sharp enough to be smeared by 20 μm ablation spots, and so the resulting recovered zonation gradients are not overly sharp. Therefore, our approach can be applied as both a means to extract additional information from datasets and also as a way to interpolate between data points. Artefacts that may be introduced by our method can be associated with noise or non-uniqueness (Fig. 5A). By changing the smoothness of the solution, noise and artefacts can be reduced however the ability to recover discrete variations also decreases. We advice that users inspect results of the analysis and perform synthetic resolution test to assess the impacts of laser spot size on their specific goals.

This approach could also be used to increase the resolution of electron microprobe data. Here the 'spot' size can be very small, however, the X-ray production volume can be large in comparison. Therefore, inverse methods would increase the resolution of this approach in the same way. Using Monte Carlo methods, we can determine how the crystal is sampled as a function of space and discretize this 3D volume in the same way as above.

Our recovered time-temperature paths for Yosemite Valley are significantly different and this could have important implications for certain applications where differentiating between geomorphic scenarios is crucial or where different thermochronometric systems yield different cooling histories. Low temperature thermal histories from high elevation (2000 m) Sierra Nevada samples have previously been constrained with fission track ages and fission track length data (Dumitru, 1990) and (U-Th)/He ages (House et al., 1997). Fission track analyses indicate rapid cooling during the latest Mesozoic to earliest Tertiary, prolonged residence at temperatures of approximately 50 °C (with large uncertainties) in the middle Tertiary, and then late Tertiary and Quaternary cooling, although this part of the history is poorly resolved by the data (Dumitru, 1990). (U-Th)/He analyses agree with early rapid cooling, however instead of a prolonged residence at relatively high

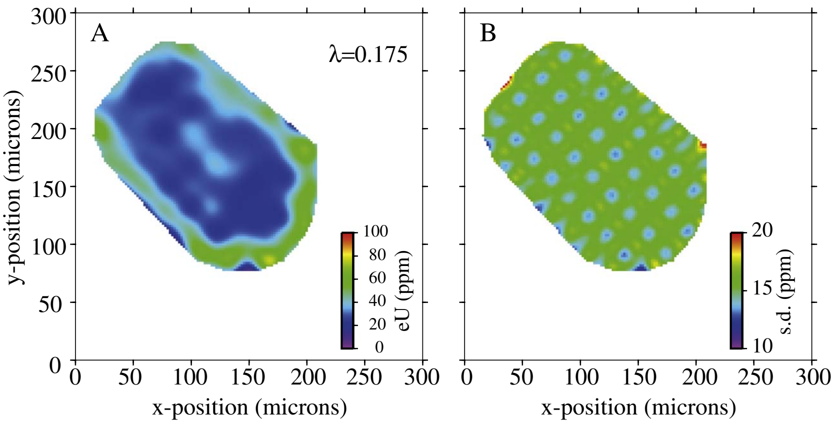

Fig. 8. Preferred zonation model. (A) Preferred zonation map of the Yosemite crystal from the data shown in Fig. 6 obtained using Eq. (13) with a λ value of 0.175. (B) Uncertainty associated with the inferred concentration map shown in (A), obtained the bootstrap method of resampling residuals with replacement. It is important to note that the uncertainty is smallest where concentration measurements have been made.

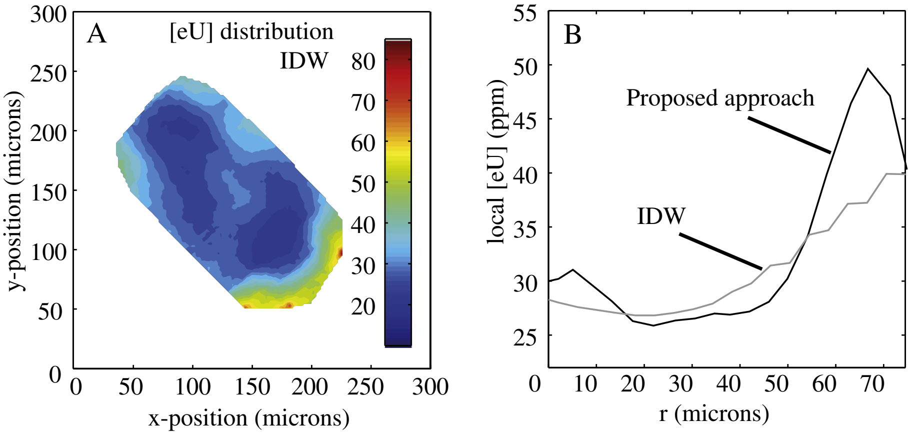

Fig. 9. Comparisons between the radially symmetric zonation models for the IDW method and our proposed approach. (A) Concentrations predicted by the inverse distance weighting (IDW) algorithm of Farley et al. (2011) through the center of spots. (B) Radially symmetric zonation obtained using the method of Farley et al. (2011) for zonation models obtained using the IDW method and the model using our inverse method. Black curve corresponds to the zonation map obtained by our inversion shown in Fig. 8. Gray curve corresponds to the zonation map obtained by IDW algorithm.

temperatures, gradual cooling is required between 70 Ma and the present from temperatures of approximately 40 °C (House et al., 1997). Part of this discrepancy may be due to a number of factors. First, problems with the calibrations of both the kinetics of fission tracks and He diffusion in apatite was suggested by House et al. (1997) to be a cause of the differences. Since the study by Dumitru (1990), fission track annealing models have been improved. In particular, the prolonged residence at 50 °C followed by recent cooling is a common artefact of earlier annealing models (Ketcham et al., 1999), suggesting that a more gradual cooling history is consistent with new annealing models. Since the study by House et al. (1997), He diffusion kinetics have been improved in apatite and now account for the influence of radiation damage and annealing to the crystal lattice (Shuster et al., 2006a,b; Shuster and Farley, 2009; Gautheron et al., 2009; Flowers et al., 2009; Fox et al., 2014). This would have the effect of increasing temperatures during the middle Tertiary compared to those recovered by House et al. (1997). Second, unaccounted for spatial variations in exhumation rate due to tilting or valley incision in the analysis of the fission track data (House et al., 1997, 2001; McPhillips and Brandon, 2012) may allow for lower temperatures during the middle Tertiary compared to those recovered by Dumitru (1990). Importantly, both earlier studies suggest that temperatures in the middle Tertiary were greater than 20 °C, and thus the recovered time-temperature path using our proposed inversion approach to interpolate LA-ICPMS data is preferred (Fig. 10).

5.1. *Magma flux timescales and model smoothness constraints*

A certain level of subjectivity is required to choose the damping parameters and this potentially has implications for the interpretation of the geological processes. The optimal value of the damping can be chosen based on a trial and error approach, or using more direct approaches by inspecting an L-curve or utilizing a reduced χ^2. Both these direct options have potential limitations. First, the L-curve is sensitive to the investigated range of the damping parameter and can lead to overly smooth models (Hanke, 1996; Vogel, 1996). Second, the reduced χ^2 approach requires that the uncertainty is accurately known, however overdispersion must be estimated and this will ultimately determine the smoothness of the solution (McLean et al., 2016).

In the case of magma flux timescales, the smoothness constraint directly controls the inferred timescale. To circumnavigate dependency on smoothness constraints for the case of inferring magma flux timescales, we can exploit prior information about the initial condition and process resulting in the observed zonation profiles. The initial condition is assumed to be a step change in Ni concentration between two zones within an olivine crystal. The processes that lead to observed gradual changes in concentration are diffusion of nickel between zones and the smearing associated with the spot size, Eq. (1). Both of these processes can be modelled and used to predict the observed data. The timescale can then be inferred using the Monte Carlo methods as presented by Ruprecht and Plank (2013). The inclusion of the smearing associated with the spot size enables shorter timescales to be inferred as presented above. Furthermore, overdispersion can also be sampled as another model parameter using the Monte Carlo algorithm. However, this approach is only suitable for simple initial conditions and does not account for the general problem of smearing due to large spot sizes.

6. Conclusions

Smearing of zonation gradients due to the large ablation spots can be overcome by explicitly accounting for the geometry of the spot size. As multiple spots may sample the same location, redundant information can be exploited to infer sub-spot size variations in concentration. This

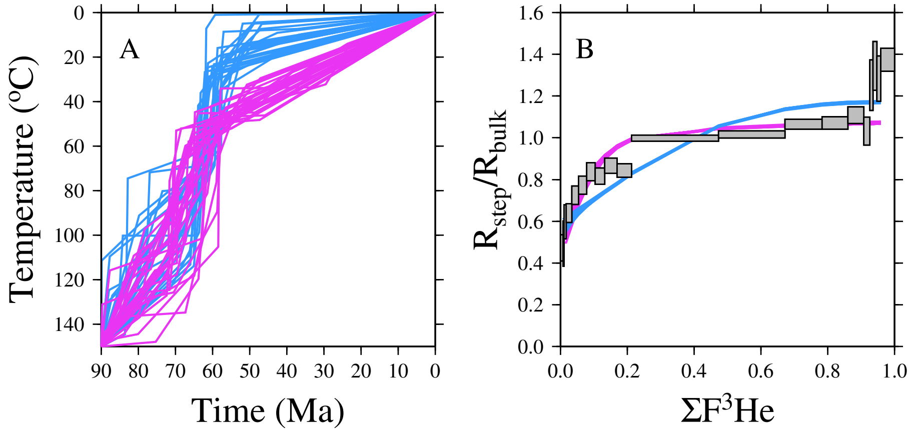

Fig. 10. Time-temperature paths that best fit the Yosemite ^{4}He/^{3}He data for the two eU zonation profiles shown in Figs. 9A and 8. (A) The 500 best fitting time temperature paths following 5000 trial time-temperature paths for both zonation models: purple paths are for the 1D radially symmetric model obtained using the inversion scheme and the blue paths are for the model obtained using the IDW approach. All paths are randomly generated with 5 time temperature nodes. (B) Corresponding predictions of ^{4}He/^{3}He evolution as a function of cumulative fraction of ^{3}He released for both zonation models. The purple paths fit the data better suggesting that the inversion scheme results in zonation models that are more realistic. (For interpretation of the references to color in this figure legend, the reader is referred to the web version of this article.)

can be achieved by using linear inverse methods allowing us to recover sharper variation is zonation. This is particularly important in problems involving diffusion, where zonation gradients are used to calculates rates of cooling. We have demonstrated this with two examples exploring cooling driven by magma ascent and surface erosion.

Our inverse method offers alternative approaches to increasing LA-ICP-MS spatial resolution. Traditionally, this resolution has been controlled by the laser spot size and this is limited by the sensitivity of the ICP-MS instrument. Instead, improved resolution could be achieved by measuring concentrations at specific locations many times with multiple laser spots centered at different locations. In turn, the objective here may be to actually increase spot size, to ablate a shallower pit to ensure that depth dependent zonation is not a factor.

Acknowledgments

Research was funded by NERC (NE/N015479/1), the NSF (EAR-1347990) from the Tectonics Program and the Ann and Gordon Getty Foundation. We thank W. Matthews and N. McLean for constructive reviews and K. Mezger for editorial assistance. We thank N. Fylstra for assistance with lab work at the Berkeley Geochronology Center. We thank G. Stock for assistance in the field. We also thank W. Sharp and K. Cuffey for stimulating discussions regarding LA-ICPMS data and deconvolving laser spots.

Appendix A. Supplementary data

Supplementary data to this article can be found online at http://dx.doi.org/10.1016/j.chemgeo.2017.07.001.

References

Bleiner, D., Günther, D., 2001. Theoretical description and experimental observation of aerosol transport processes in laser ablation inductively coupled plasma mass spectrometry. J. Anal. At. Spectrom. 16 (5), 449–456.

Boyce, J., Hodges, K., 2005. U and Th zoning in Cerro de Mercado (Durango, Mexico) fluorapatite: insights regarding the impact of recoil redistribution of radiogenic ^{4}He on (U-Th)/He thermochronology. Chem. Geol. 219 (1), 261–274.

Bussweiler, Y., Foley, S.F., Prelević, D., Jacob, D.E., 2015. The olivine macrocryst problem: new insights from minor and trace element compositions of olivine from Lac de Gras kimberlites, Canada. Lithos 220, 238–252.

Constable, S.C., Parker, R.L., Constable, C.G., 1987. Occam's inversion: a practical algorithm for generating smooth models from electromagnetic sounding data. Geophysics 52 (3), 289–300.

Costa, F., Chakraborty, S., Dohmen, R., 2003. Diffusion coupling between trace and major elements and a model for calculation of magma residence times using plagioclase. Geochim. Cosmochim. Acta 67 (12), 2189–2200.

Cottle, J., Horstwood, M., Parrish, R.R., 2009. A new approach to single shot laser ablation analysis and its application to in situ Pb/U geochronology. J. Anal. At. Spectrom. 24 (10), 1355–1363.

Davidson, J.P., Morgan, D.J., Charlier, B.L.A., Harlou, R., Hora, J.M., 2007. Microsampling and isotopic analysis of igneous rocks: implications for the study of magmatic systems. Annu. Rev. Earth Planet. Sci. 35, 273–311.

Devroye, L., 1986. Non-Uniform Random Variate Generation (Originally Published With. Springer-Verlag.

Dumitru, T.A., 1990. Subnormal Cenozoic geothermal gradients in the extinct Sierra Nevada magmatic arc: consequences of laramide and post-laramide shallow-angle subduction. J. Geophys. Res. Solid Earth 95 (B4), 4925–4941.

Efron, B., 1979. Bootstrap methods: another look at the jackknife. Ann. Stat. 7 (1), 1–26.

Farley, K.A., Shuster, D.L., Ketcham, R.A., 2011. U and Th zonation in apatite observed by laser ablation ICPMS, and implications for the (U-Th)/He system. Geochim. Cosmochim. Acta 75 (16), 4515–4530.

Farley, K.A., Shuster, D.L., Watson, E.B., Wanser, K.H., Balco, G., 2010. Numerical investigations of apatite ^{4}He/^{3}He thermochronometry. Geochem. Geophys. Geosyst. 11 (10).

Farley, K.A., Wolf, R.A., Silver, L.T., 1996. The effects of long alpha-stopping distances on (U-Th)/He ages. Geochim. Cosmochim. Acta 60, 4223–4229 Nov.

Flowers, R.M., Farley, K.A., 2012. Apatite ^{4}He/^{3}He and (U-Th)/He evidence for an ancient Grand Canyon. Science 338 (6114), 1616–1619.

Flowers, R.M., Ketcham, R.A., Shuster, D.L., Farley, K.A., 2009. Apatite (U-Th)/He thermochronometry using a radiation damage accumulation and annealing model. Geochim. Cosmochim. Acta 73 (8), 2347–2365.

Fox, M., Ickert, R.B., 2015. Model selection during sample-standard-bracketing using reversible jump Markov Chain Monte Carlo. J. Anal. At. Spectrom. 30 (10), 2208–2213.

Fox, M., McKeon, R.E., Shuster, D.L., 2014. Incorporating 3-D parent nuclide zonation for apatite ^{4}He/^{3}He thermochronometry: an example from the Appalachian Mountains. Geochem. Geophys. Geosyst. 15 (11), 4217–4229.

Fox, M., Shuster, D.L., 2014. The influence of burial heating on the (U-Th)/He system in apatite: Grand Canyon case study. Earth Planet. Sci. Lett. 397, 174–183.

Gäckle, M., Merten, D., 2005. Modelling the temporal intensity distribution in laser ablation-inductively coupled plasma-mass spectrometry (LA-ICP-MS) using scanning and drilling mode. Spectrochim. Acta B At. Spectrosc. 60 (12), 1517–1530.

Gallagher, K., Sambridge, M., 1992. The resolution of past heat flow in sedimentary basins from non-linear inversion of geochemical data: the smoothest model approach, with synthetic examples. Geophys. J. Int. 109 (1), 78–95.

Gautheron, C., Tassan-Got, L., Barbarand, J., Pagel, M., 2009. Effect of alpha-damage annealing on apatite (U-Th)/He thermochronology. Chem. Geol. 266 (3), 157–170.

Goren, L., Fox, M., Willett, S.D., 2014. Tectonics from fluvial topography using formal linear inversion: theory and applications to the Inyo Mountains, California. J. Geophys. Res. Earth 119 (8), 1651–1681.

Hanke, M., 1996. Limitations of the L-curve method in ill-posed problems. BIT Numer. Math. 36 (2), 287–301.

Hansen, P.C., 1992. Analysis of discrete ill-posed problems by means of the L-curve. SIAM review 34 (4), 561–580.

House, M., Wernicke, B., Farley, K., Dumitru, T., 1997. Cenozoic thermal evolution of the central Sierra Nevada, California, from (UTh)/He thermochronometry. Earth Planet. Sci. Lett. 151 (3-4), 167–179.

House, M.A., Wernicke, B.P., Farley, K.A., 2001. Paleo-geomorphology of the Sierra Nevada, California, from (U-Th)/He ages in apatite. Am. J. Sci. 301 (2), 77–102.

Ketcham, R.A., Donelick, R.A., Carlson, W.D., 1999. Variability of apatite fission-track annealing kinetics: III. Extrapolation to geological time scales. Am. Mineral. 84 (9), 1235–1255.

Lasaga, A.C., Jiang, J., 1995. Thermal history of rocks; PTt paths for geospeedometry, petrologic data, and inverse theory techniques. Am. J. Sci. 295 (6), 697–741.

McLean, N.M., Bowring, J.F., Gehrels, G., 2016. Algorithms and software for U-Pb geochronology by LA-ICPMS. Geochem. Geophys. Geosyst. 17 (7), 2480–2496.

McPhillips, D., Brandon, M.T., 2012. Topographic evolution of the Sierra Nevada measured directly by inversion of low-temperature thermochronology. Am. J. Sci. 312 (2), 90–116.

Menke, W., 2012. Geophysical Data Analysis: Discrete Inverse Theory. vol. 45 Academic Press.

Morgan, D.J., Jollands, M.C., Lloyd, G.E., Banks, D.A., 2014. Using titanium-in-quartz geothermometry and geospeedometry to recover temperatures in the aureole of the Ballachulish Igneous Complex, NW Scotland. Geol. Soc. Lond., Spec. Publ. 394 (1), 145–165.

Mouchi, V., Crowley, Q.G., Ubide, T., 2016. AERYN: a simple standalone application for visualizing and enhancing elemental maps. Appl. Geochem. 75, 44–53.

Ortolano, G., Zappalà, L., Mazzoleni, P., 2014. X-ray map analyser: a new arcGIS® based tool for the quantitative statistical data handling of X-ray maps (geo-and material-science applications). Comput. Geosci. 72, 49–64.

Paul, B., Paton, C., Norris, A., Woodhead, J., Hellstrom, J., Hergt, J., Greig, A., 2012. CellSpace: a module for creating spatially registered laser ablation images within the Iolite freeware environment. J. Anal. At. Spectrom. 27 (4), 700–706.

Plotnikov, A., Vogt, C., Wetzig, K., 2002. An approach to the reconstruction of true concentration profile from transient signal in spatially resolved analysis by means of laser ablation ICP MS. J. Anal. At. Spectrom. 17 (9), 1114–1120.

Rittner, M., Müller, W., 2012. 2D mapping of LA-ICPMS trace element distributions using R. Comput. Geosci. 42, 152–161.

Ruprecht, P., Plank, T., 2013. Feeding andesitic eruptions with a high-speed connection from the mantle. Nature 500 (7460), 68–72.

Sambridge, M., 1990. Non-linear arrival time inversion: constraining velocity anomalies by seeking smooth models in 3-D. Geophys. J. Int. 102 (3), 653–677.

Segall, P., Harris, R., 1987. Earthquake deformation cycle on the San Andreas Fault near Parkfield, California. J. Geophys. Res. Solid Earth 92 (B10), 10511–10525.

Shuster, D., Flowers, R., Farley, K., 2006a. Radiation damage and helium diffusion kinetics in apatite. Geochim. Cosmochim. Acta 70 (18), A590.

Shuster, D.L., Ehlers, T.A., Rusmoren, M.E., Farley, K.A., 2005. Rapid glacial erosion at 1.8 Ma revealed by ^{4}He/^{3}He thermochronometry. Science 310 (5754), 1668–1670.

Shuster, D.L., Farley, K.A., 2004. ^{4}He/^{3}He thermochronometry. Earth Planet. Sci. Lett. 217 (1), 1–17.

Shuster, D.L., Farley, K.A., 2009. The influence of artificial radiation damage and thermal annealing on helium diffusion kinetics in apatite. Geochim. Cosmochim. Acta 73 (1), 183–196.

Shuster, D.L., Flowers, R.M., Farley, K.A., 2006b. The influence of natural radiation damage on helium diffusion kinetics in apatite. Earth Planet. Sci. Lett. 249 (3), 148–161.

Snieder, R., Trampert, J., 1999. Inverse problems in geophysics. In: Wavefield Inversion. Springer, pp. 119–190.

Streck, M.J., 2008. Mineral textures and zoning as evidence for open system processes. Rev. Mineral. Geochem. 69 (1), 595–622.

Tarantola, A., 2005. Inverse Problem Theory and Methods for Model Parameter Estimation. Society for Industrial and Applied Mathematics.

Tremblay, M.M., Fox, M., Schmidt, J.L., Tripathy-Lang, A., Wielicki, M.M., Harrison, T.M., Zeitler, P.K., Shuster, D.L., 2015. Erosion in southern Tibet shut down at ~10 Ma due to enhanced rock uplift within the Himalaya. Proc. Natl. Acad. Sci. 112

(39), 12030–12035.

Tripathy-Lang, A., Fox, M., Shuster, D.L., 2015. Zircon ^{4}He/^{3}He thermochronometry. Geochim. Cosmochim. Acta 166, 1–14.

Ubide, T., McKenna, C.A., Chew, D.M., Kamber, B.S., 2015. High-resolution LA-ICP-MS trace element mapping of igneous minerals: in search of magma histories. Chem. Geol. 409, 157–168.

Vermeesch, P., 2015. Revised error propagation of ^{40}Ar/^{39}Ar data, including covariances. Geochim. Cosmochim. Acta 171, 325–337.

Vogel, C.R., 1996. Non-convergence of the L-curve regularization parameter selection method. Inverse Prob. 12 (4), 535.

Woodhead, J.D., Hellstrom, J., Hergt, J.M., Greig, A., Maas, R., 2007. Isotopic and elemental imaging of geological materials by laser ablation inductively coupled plasma-mass spectrometry. Geostand. Geoanal. Res. 31 (4), 331–343.